Lawrence Berkeley National Laboratory
Lawrence Berkeley National Laboratory

Title
Fracture imaging with converted elastic waves

Permalink
https://escholarship.org/uc/item/8668w148

Authors
Nihei, K.T.
Nakagawa, S.
Myer, L.R.

Publication Date
2001-05-29

Fracture imaging with converted elastic waves

K.T. Nihei, S. Nakagawa & L.R. Myer
Lawrence Berkeley National Laboratory, Berkeley, California, USA

ABSTRACT: This paper examines the seismic signatures of discrete, finite-length fractures, and outlines an approach for elastic, prestack reverse-time imaging of discrete fractures. The results of this study highlight the importance of incorporating fracture-generated *P-S* converted waves into the imaging method, and presents an alternate imaging condition that can be used in elastic reverse-time imaging when a direct wave is recorded (e.g., for crosswell and VSP acquisition geometries).

1 INTRODUCTION

The presence of natural and induced fractures in reservoir rock can significantly enhance oil and gas production, especially in tight formations. Additionally, fractures in rock engineering projects represent planes of mechanical weakness that can compromise the integrity of engineered structures built within the rock mass. Thus, a priori knowledge of the locations, orientations, and mechanical stiffnesses of fractures is desirable for the optimization of oil and gas production and in the design of safe underground structures.

Over the last decade, seismic methods have been used increasingly to determine fracture orientation and density (e.g., for reviews, see Tsvankin and Lynn, 1999, and MacBeth and Lynn, 2000). These methods typically assume that the fracture spacing is small relative to the seismic wavelength. When this assumption is valid, it is possible to utilize effective medium theories to compute the (zero frequency) equivalent anisotropic properties of the fractured rock mass. Seismic methods for characterization of fractured rock utilize the predictions from these equivalent anisotropic models (e.g., non-hyperbolic normal moveout, split shear waves, direction-dependent amplitude versus azimuth) to obtain estimates of fracture density and orientation.

With the continued development of higher frequency borehole sources and sensors for crosswell and singlewell data acquisition, the potential for imaging discrete fractures and fracture zones using higher frequency waves is becoming evident (Majer et al., 1997; Coates et al., 1998). The objective of this research is to identify potentially diagnostic seismic signatures of finite length fractures, and to develop methods that utilize these signatures to image fractures.

This paper begins with a discussion of the factors controlling the seismic visibility of discrete, finite-length fractures with a particular focus on the generation of *P-S* fracture converted waves. This section is followed by the description of an approach for modeling finite-length fractures with an anisotropic finite difference code. Snapshots of *P-S* conversions generated on a finite-length, fluid-filled, open fracture are presented. These results motivated the development of an elastic, full-waveform fracture imaging approach based on the reverse-time migration concept. Here, we introduce a variant of the excitation-time imaging condition (Chang and McMechan, 1986) suited for transmission imaging (e.g., crosswell and VSP) in which the backpropagated direct wave, rather than the forward propagated wave from the source, is used in the reverse-time imaging process. A numerical example for a simple vertical fracture model is given.

2 SEISMIC VISIBILITY OF DISCRETE, FINITE-LENGTH FRACTURES

Two geometric factors control the magnitude of converted waves generated by a discrete, finite-length fracture: the fracture length *l,* and the *equivalent background thickness* of the fracture ℓ (Haugen and Schoenberg, 2000). Numerical simulations of finite length fractures (Nihei et al., 2000) indicate that the fracture length should be greater than approximately one half of the *P*-wave wavelength to generate appreciable *P-S* converted waves, i.e., a dimension-
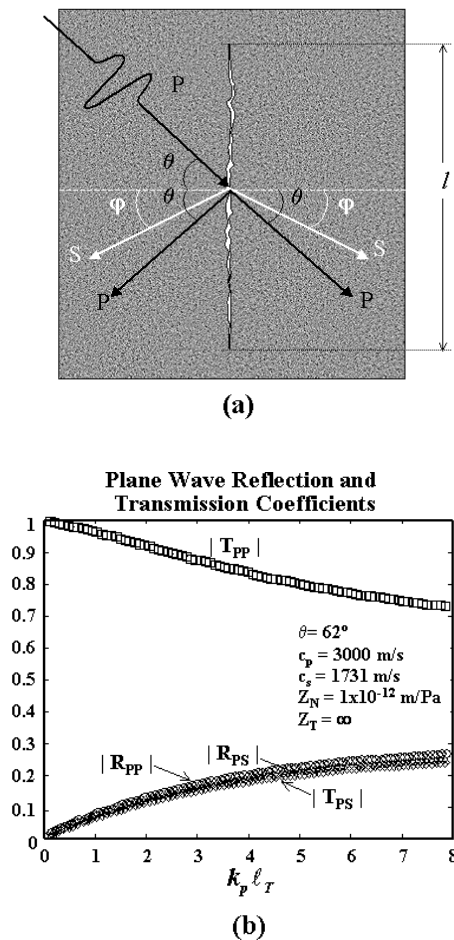
(a)

(b)

Figure 1. Plane wave transmission and reflection at a single fracture: (a) *P*-wave incident upon the fracture at 62°, and (2) transmission and reflection coefficients (assuming an infinitely long fracture) for the *P-P* and *P-S* transmitted and reflected waves computed as a function of the dimensionless wavenumber.

less wavenumber of magnitude $k_P l > 3$, where k_P is the *P*-wave wavenumber and l is the length of the fracture (Fig. 1a).

The influence of the fracture properties on the generation of converted *S*-waves by an incident *P*-wave is determined by a second dimensionless wavenumber $k_P \ell_T$, where $\ell_T = Z_T \mu$ is the tangential equivalent thickness of the fracture (Haugen and Schoenberg, 2000), Z_T is the fracture tangential compliance, and μ is the shear modulus of the host rock. Physically, ℓ_T represents the thickness of the host medium required to achieve the same shear deformation as that taking place across the fracture As Haugen and Schoenberg point out, ℓ_T is a static property of the fracture with dimensions of length that can be an order of magnitude greater than the physical width of the fracture.

Developing a rule of thumb for the magnitude of $k_P \ell_T$ required for detectable *P-S* fracture converted waves is complicated by an angle dependency of the converted wave reflection and transmission coefficients that is not included in this simple dimensionless quantity. For the specific example considered later in this paper (fluid-filled, open fracture

with a *P*-wave incident at 62°; Fig. 1a), the magnitude of $k_P \ell_T$ required to generate *P-S* converted waves can be estimated from the plane wave reflection and transmission coefficients for a single, infinitely long fracture (e.g., Schoenberg, 1980; Pyrak-Nolte et al., 1990; Gu et al., 1996a), as shown in Figure 1b. Examination of the *P-S* reflection and transmission coefficients in Figure 1b shows that *P-S* converted waves with amplitudes approximately 10% to 30% of the incident *P*-wave are produced when $k_P \ell_T > 1$.

3 ANISOTROPIC REPRESENTATION OF DISCRETE FRACTURES

3.1 Discrete fracture modeling

Natural fractures in sedimentary rocks often appear as vertical planes of compliance with spacings on the order of the bed thickness. It is well established that the seismic properties of rock containing sets of aligned fractures can be modeled by an equivalent anisotropic medium, provided the wavelength is large relative to the fracture spacing and the equivalent thickness of the fracture ℓ described in the preceding section (Schoenberg and Sayers, 1995). If either of these conditions is violated, wave interaction with the fracture becomes more complex, e.g., frequency-dependent body wave reflection, transmission, and conversion (Schoenberg, 1980; Pyrak-Nolte et al., 1990), fracture interface waves (Pyrak-Nolte et al., 1992), fracture head waves (Gu et al., 1996b), and fracture channel waves (Nakagawa, 1998; Nihei et al., 1999).

The numerical modeling of seismic waves in a rock mass with discrete, finite-length fractures requires an efficient and accurate numerical approach that is capable of modeling many fractures and realistic strata. Boundary element approaches probably offer the highest accuracy and flexibility for modeling discrete, finite-length fractures. Fractures can be modeled explicitly as displacement-jump boundary conditions (Eq. 2) with spatially varying fracture compliances (Gu et al., 1996b). Additionally, special crack tip boundary elements have been developed to preserve the singular nature of the stress field at the tips of the fracture. A current limitation of boundary element methods, however, is the matrix storage requirements for models with multiple fractures and multiple rock types.

A recent paper by Coates and Schoenberg (1995) has demonstrated that it is possible to accurately model discrete fractures in an explicit finite difference code. This approach is fast computationally and is capable of modeling complex strata. In the following, we describe the Coates-Schoenberg approach and discuss our efforts to use this approach to model seismic wave propagation in a medium containing finite-length fractures.

3.2 Coates-Schoenberg approach for discrete fracture modeling

Discrete fracture modeling is performed using an explicit, anisotropic finite difference code based on the staggered grid method with 4th order accuracy in space and 2nd order accuracy in time. By allowing the medium to be monoclinic, individual fractures can be represented as compliant zones of a single cell thickness (Fig. 2) and with properties described by their elastic constants (six in 2-D), as presented by Coates and Schoenberg (1995). The process for obtaining the anisotropic elastic constants for the finite difference cells representing the fracture is based on a calculation of the average strain of each cell (Schoenberg and Sayers, 1995)

$$\varepsilon_{ij}^{cell} = s_{ijkl}^{b}\sigma_{kl} + \frac{1}{2L}([u_i]n_j + [u_j]n_i),\qquad(1)$$

where s_{ijkl}^{b} is the compliance of the host rock, σ_{kl} is the stress, $[u_i]$ is the displacement jump across the fracture (i.e., the displacement-discontinuity or crack opening displacement), L is the length of the cell, and n_i is the fracture normal vector.
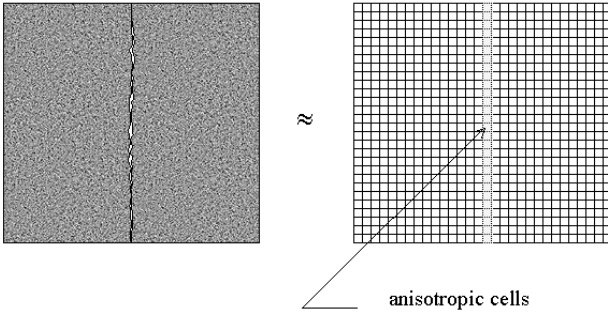

Figure 2. Representation of a discrete, vertical fracture in a finite difference model as a single column of anisotropic cells. The elastic constants for these cells are computed using the Coates-Schoenberg approach described in the text.

Assuming that the applied traction $\sigma_{jk} n_k$ and the resulting displacement jump $[u_i]$ are linearly-related through a constant Z_{ij},

$$[u_i] = Z_{ij}\sigma_{jk} n_k,\qquad(2)$$

Equation 1 becomes

$$\varepsilon_{ij}^{cell} = s_{ijkl}^{b}\sigma_{kl}$$
$$+ \frac{1}{4L}(Z_{ik}n_l n_j + Z_{jk}n_l n_i + Z_{il}n_k n_j + Z_{jl}n_k n_i)\sigma_{kl} \quad(3)$$
$$\equiv s_{ijkl}^{cell}\sigma_{kl}.$$

Here, s_{ijkl}^{cell} are the anisotropic compliances for the cell containing the fracture.

The compliance matrix given in Equation 3 can be inverted to give the anisotropic elastic constants for the cell. For a vertical fracture with its normal in the 1-direction, the 4 independent anisotropic elastic constants for a 2-D model in the 1-3 plane are (in abbreviated notation)

$$c_{IJ}^{cell} = \begin{bmatrix} (\lambda+2\mu)(1-\delta_N) & \lambda(1-\delta_N) & 0 \\ \lambda(1-\delta_N) & (\lambda+2\mu)(1-r^2\delta_N) & 0 \\ 0 & 0 & \mu(1-\delta_T) \end{bmatrix},(4)$$

where

$$r = \nu/(1-\nu),$$
$$\delta_N = Z_N(\lambda+2\mu)/[L+Z_N(\lambda+2\mu)],\qquad(5)$$
$$\delta_T = Z_T\mu/(L+Z_T\mu),$$

and ν, λ, and μ are the Poisson's ratio, Lamé constant and shear modulus of the host rock, Z_N and Z_T are the normal and shear fracture compliances, and L is the length of the finite difference cell. Equation 4 describes the fracture as a transversely isotropic material with a horizontal axis of symmetry (HTI material). Because individual fractures are described by their elastic constants, multiple discrete fractures with any specified normal and shear fracture compliances can be easily modeled. Fractures oriented at an angle to the finite difference grid can also be modeled by applying a rotation transformation to Equation 4, as described by Coates and Schoenberg (1995).

3.3 Modeling finite-length fractures

Finite-length fractures are currently being modeled using the Coates-Schoenberg finite difference approach outlined in the previous section by simply truncating the fracture without any special considerations for the fracture tips. The physical meaning of this type of fracture tip model within the context of elliptical versus cusp-shaped crack opening displacements (i.e., elastic crack tip model versus Dugdale-Barenblatt elasto-plastic crack tip model; Kanninen and Popelar, 1985) is the subject of ongoing research. This issue may be somewhat academic, however, because the numerical simulations shown here indicate that the fracture tip diffracted waves are not the dominant signature of the fracture for waves recorded in the far-field.

The results for a finite-length fracture generated by the finite difference approach have been compared with a 2-D elastic boundary element code (multi-region formulation) in which the fracture is modeled using the displacement jump boundary condition described by Equation 2. Qualitative comparisons show good agreement for the body wave phases with small differences in the amplitudes of the various crack-tip diffracted phases (Fig. 3).

The effects of a single, vertical, finite-length fracture on an incident P-wave wave were examined using the finite difference method. The incident P-wave is generated by a 100 Hz explosion source.

Single Fracture Finite Difference Simulation: Time Step = 0.1 s
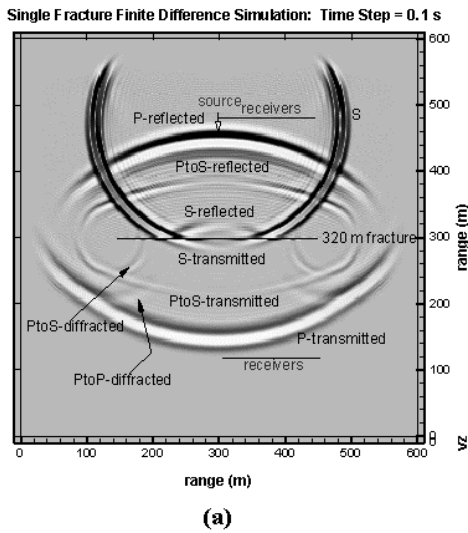
(a)

vertical component, v$_z$
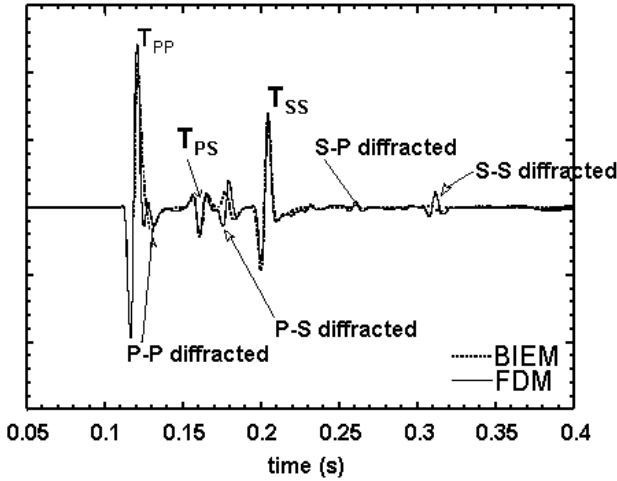
(b)

Figure 3. Comparison between the finite difference method and boundary element method for modeling 2-D elastic wave propagation across a single fracture: (a) fracture model with snapshot of the vertical particle velocity superimposed, and (b) vertical component of the particle velocity computed using the two numerical methods. The receiver is located 200 m below the right fracture tip. The source is a 100 Hz Ricker wavelet oriented in the −z direction. The fracture is 320 m long with normal and shear compliances equal to 7.16×10^{-10} m/Pa.

The fracture is 54.4 m in length and was assigned properties representative of an open, fluid-filled fracture ($Z_N \square 0$, $Z_T \to \infty$). The velocities in the model are 3000 m/s and 1731 m/s for the P- and S-waves, respectively, and the density is 2100 kg/m^3.

Figures 4a,c display the vertical component of the particle velocity for two source locations. When the source is located off the fracture plane (Fig. 4b), the incident P-wave generates converted P-S reflected and P-S transmitted waves. The magnitude of these waves appears much larger than the fracture tip diffracted waves. When the source is located directly above the fracture, the converted waves are no longer excited (Fig. 4a). For this case of grazing incidence, we have found that it is possible to excite a P-S fracture head wave, but only when the fracture has a non-zero normal compliance (i.e., $Z_N > 0$), as
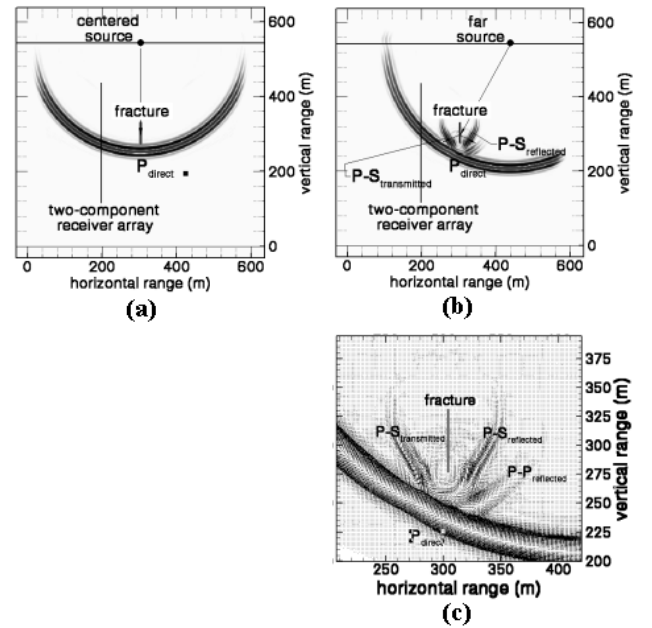

(a) **(b)**

(c)

Figure 4. Snapshots of the vertical particle velocity produced by a 100 Hz explosion source for three source-receiver offsets: (a) fracture-centered source, and (b) offset source (angle of incidence is 62°). The fracture is 54.4 m in length with normal and shear fracture compliances $Z_N \square 0$ and $Z_T \to \infty$, representative of an open, fluid-filled fracture. An expanded view of (b) is shown as a vector plot in (c). The magnitudes of the fracture-converted waves are near-equal, as predicted by plane wave theory (Fig. 1b).

might be the case for a gas-filled fracture (case not shown).

An expanded view of the wavefield of Figure 4b is displayed as a vector plot of the particle velocities in Figure 4c. Faint evidence of fracture tip diffractions and fracture interface waves are present, with the dominant P-S converted waves along with a P-P reflection. The basic character of the wavefield suggests that the dominant seismic signatures for this particular problem geometry and fracture properties are the converted P-S waves. For this particular model, the amplitudes of the transmitted and reflected P-S waves and the reflected P-P wave have similar magnitudes, as predicted by plane wave theory (Fig. 1b).

4   ELASTIC REVERSE-TIME IMAGING WITH FRACTURE CONVERTED WAVES

Crosswell, singlewell, and vertical seismic profiling (VSP) methods hold great promise for discrete fracture/fracture zone imaging because of the potential for using higher frequency sources and placing receivers close to the fractures. In this section, we will outline a basic strategy for imaging fractures using fracture-converted waves and a VSP acquisition geometry.

The approach for imaging fractures described here is an adaptation of the excitation-time imaging condition used in reverse-time migration (Chang and

McMechan, 1986, 1987) to acquisition geometries in which a direct wave is recorded (e.g., crosswell and VSP). In the excitation-time imaging approach, the wavefield recorded at the receiver array is first processed to mute out the direct wave, and then time-reversed and propagated back into the medium (i.e., backpropagation of the scattered wavefield). Concurrently, the wavefield from the source is forward propagated into the medium. An image of the scatterers is formed by multiplying the source-forward propagated and receiver-backpropagated wavefields at each time step and adding the current image to the images obtained at earlier time steps to form a composite image.

A practical limitation of this approach is it's required knowledge of the source characteristics, such as the source time function, the source radiation pattern, and the source-medium coupling, that may not be available. Imaging can be performed without knowledge of the source properties if a direct wave is recorded. The basic scheme is as follows:

(1) separate the direct wave particle velocity wavefield v_i° from the coda particle velocity wavefield v_i^s,

(2) assume an average velocity model of the subsurface or incorporate a more precise velocity model if this information is available from well logs or other sources,

(3) separately backpropagate v_i° and v_i^s one time step by applying these as sources in separate finite difference runs in time-reversed fashion (i.e., last in, first out),

(4) construct images of heterogeneities that generated the P-S converted waves by forming the product of the divergence and curl of the backpropagated wavefields v_i° and v_i^s (i.e.,$[div(v_i^\circ)] \cdot [curl(v_i^s)]$) at each point in the finite difference model,

(5) repeat steps 3 and 4, summing the image formed at each time step with the image from the previous time step to form a composite image displaying the locations and scattering strengths of the heterogeneities.

(6) for multiple source locations, repeat steps 1 through 5 and sum the composite images formed for each source.

The motivation for forming the image of the fracture using the product $[div(v_i^\circ)] \cdot [curl(v_i^s)]$ is that the first operation isolates the P-wave wavefront (i.e., the source wavefield) and the second operation isolates the S-wave wavefront(s) (i.e., the converted S-wavefield generated at the fracture). Taking the product of these two fields produces an image at the point where the incident P-wave generates the S-wave (i.e., at the fracture).

It should be noted that a formal mathematical basis for image formation via a zero-lag time correla-

tion of backpropagated wavefields can be found in the gradient-based, full-waveform nonlinear inversion method of Tarantola (1988). This approach uses an adjoint state development to derive an expression for the gradient describing the change in the L_2 norm of the data residuals (i.e., the difference between model predicted and measured particle displacements) that results from a change in the elastic constants. The expression for the gradient (assuming the Born approximation is valid) is found to be the zero-lag cross-correlation of the strains of the forward propagated wavefield from the source with the strains of the backpropagated residual wavefield from the receiver locations.
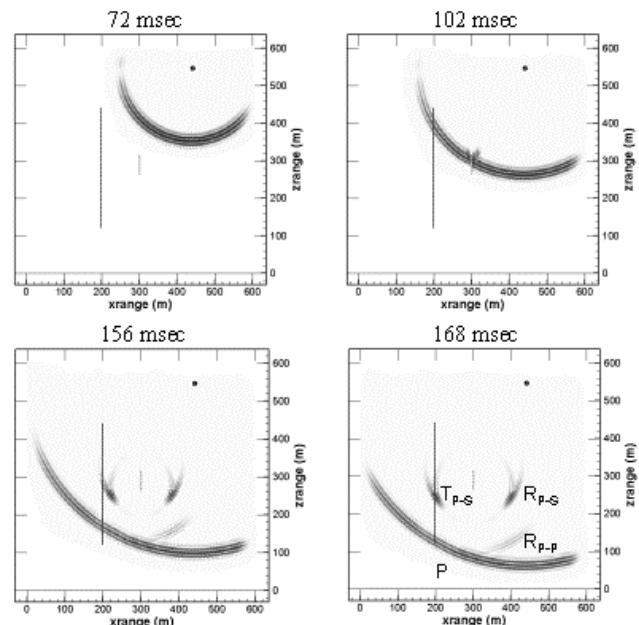

Figure 5. Snapshots of the vertical particle velocity illustrating the various arrivals that will be recorded along the 320 m long, two-component receiver array. The 100 Hz explosion source is located 240 m from the receiver borehole. The model properties are the same as those used in Figure 4b.

5 VSP EXAMPLE

In this section, the elastic reverse-time fracture imaging scheme described in the previous section is applied to the single fracture VSP model of Figure 4b. Snapshots of the vertical component of the particle velocity for the forward model are displayed in Figure 5. The last snapshot at 168 msec shows three arrivals sweeping across the receiver array. The first to arrive is the direct P-wave. The P-wave is followed by a fracture converted P-S wave and a small P-S diffracted wave off the lower fracture tip.

The particle velocities recorded along the receiver array (for every other receiver) are displayed in Figure 6 after they have been separated into the direct P-wave and coda parts (step 1 of the imaging scheme). The direct P-wave and refracted P-S fractured converted wave are clear on the incident and "scattered" traces. These traces are input into sepa-

rate finite difference models. Each receiver becomes a boundary condition source that fires two components of particle velocity as specified by the recorded data after it has been time-reversed (i.e., so the last wave in is the first wave out; step 3 of the imaging scheme). Snapshots of the time-reversed, backpropagated wavefields for three time steps are shown in Figure 7. These snapshots should be compared to their analogs for forward propagation shown in Figure 5.
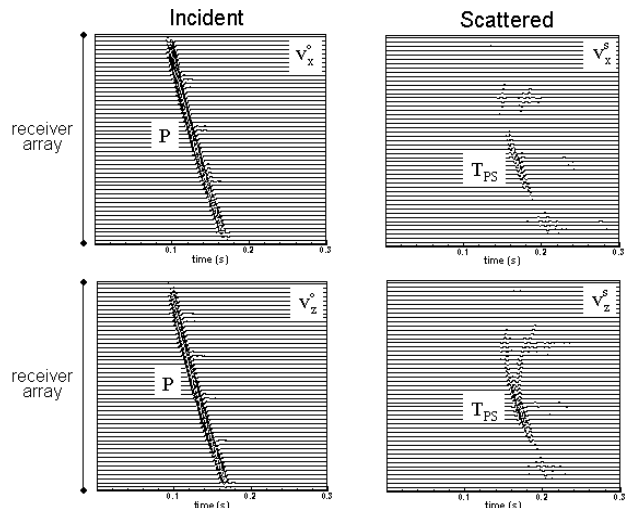

Figure 6. Traces recorded along the receiver array after separation into the direct P-wave and its coda. The arrivals on these traces correspond to the snapshots shown in Figure 5.
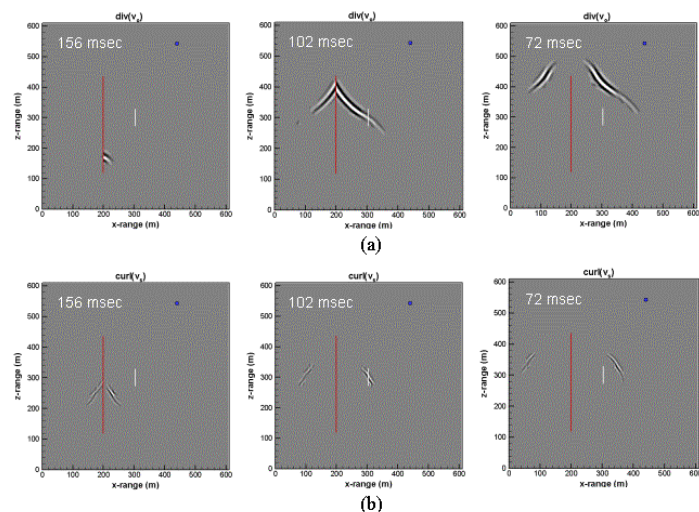

Figure 7. Time-reversed, backpropagated wavefields at three time steps (156, 102, 72 msec): (a) $\mathrm{div}(v_i^\circ)$, and (b) $\mathrm{curl}(v_i^s)$.

The image of the fracture was formed using 100 two-component particle velocity receivers spaced every 3.2 m along a vertical profile. The location and extent of the fracture are recovered in the image formed by taking the product $[\mathrm{div}(v_i^\circ)] \cdot [\mathrm{curl}(v_i^s)]$ (Fig. 8; steps 4 and 5 of the imaging scheme).

6 SUMMARY AND CONCLUSIONS

In this paper, we have described an approach for modeling discrete, finite-length fractures based on the Coates and Schoenberg (1995) approach. Individual fractures are modeled as single-thickness anisotropic cells in a staggered grid finite difference code. The properties of these cells can be directly related to the normal and shear fracture compliances.
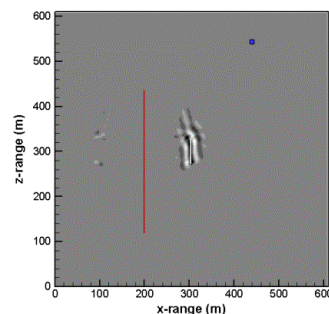

Figure 8. Image of fracture formed using the elastic reverse-time imaging scheme described in the text. The data used in the imaging are two-component particle velocities recorded at 100 receivers generated by a single 100 Hz explosion source located 240 m from the receiver borehole.

Numerical tests using this code have demonstrated that the dominant arrivals generated on finite-length fractures are the reflected and refracted body waves. For an incident P-wave, the diffracted waves are usually much smaller than the transmitted and reflected P-S and reflected P-P waves.

Elastic reverse-time fracture imaging can be performed using the converted waves by separately backpropagating the incident and "scattered" particle velocities fields in two separate staggered grid finite difference codes, and forming the time integrated product of $\mathrm{div}(v_i^\circ)$ and $\mathrm{curl}(v_i^s)$ at each cell.

As discussed previously, the reverse-time imaging approach outlined here does not use the forward propagated wave from the source in the imaging process. This is beneficial from two standpoints: (1) it avoids difficulties associated with source properties estimation (e.g., source time function, source radiation pattern, source-medium coupling), and (2) it avoids the time required to propagate the wavefield from the source to the imaging region. With regard to the latter point, the method presented here is more local to the receiver array and, therefore, requires a smaller finite difference model for the backpropagations.

The method, however, does have some restrictions and limitations. Firstly, it is only applicable to source-receiver acquisition geometries where a direct wave is recorded (e.g., for crosswell and VSP acquisition geometries). Secondly, the method utilizes forward scattered waves, and, thus, will not image reflectors that are located outside a cone of the forward scattered wavefield (e.g., reflectors beneath the receiver array). The latter point is probably not a severe restriction, and future research will investigate the spatial coverage of this reverse-time imaging approach. Future work is also planned to test the approach on more complex models including layer-

ing and multiple fractures, and on laboratory and field data.

ACKNOWLEDGMENTS

REFERENCES

Chang, W.-F. & McMechan, G.A. 1986. Reverse-time migration of offset vertical seismic profiling data using the excitation-time imaging condition. *Geophys.* 51:67-84.

Chang, W.-F. & McMechan, G.A. 1987. Elastic reverse-time migration. *Geophys.* 52, 1365-1375.

Coates, R.T. & Schoenberg, M., 1995, Finite-difference modeling of faults and fractures. *Geophys.* 60:1514-1526.

Coates, R., Kane, M., Chang, C., Hoyle, D., Watanabe, S., Dodds, K., Esmersoy, C. & Foreman, J. 1998. Localized maps of the subsurface. *Schlumberger Oilfield Review* 10(1):56-66.

Gu, B.L., Suarez-Rivera, R., Nihei, K.T. & Myer, L.R. 1996a. Incidence of plane waves upon a fracture. *J. Geophys. Res.* 101:25337-25346.

Gu, B.L., Nihei, K.T., Myer, L.R. & Pyrak-Nolte, L.J. 1996b. Numerical simulation of elastic wave propagation in fractured rock with the boundary integral equation method. *J. Geophys. Res.* 101:15933-15943.

Haugen, G.U. & Schoenberg, M.A. 2000. The echo of a fault or fracture. *Geophys.* 65(1):176-189.

Kanninen, M.F. & Popelar, C.H. 1985. *Advanced Fracture Mechanics* Oxford:Oxford.

MacBeth, C. & Lynn, H.B. 2000. Fracture-related reflectivity. in *Applied Seismic Anisotropy: Theory, Background, and Field Studies*, Soc. Expl. Geophys. Geophysics Reprint Series No. 20:233-235.

Majer, E.L., Peterson, J.E., Daley, T.M., Kaelin, B., Myer, L., Queen, J., D'Onfro, P. & Rizer, W. 1997. Fracture detection using crosswell and singlewell surveys. *Geophys.* 62:495-504.

Nakagawa, S. 1998. *Acoustic Resonance Characteristics of Rock and Concrete Containing Fractures*. Ph.D. Thesis, 383 pp., Univ. of California at Berkeley.

Nihei, K.T., Schoenberg, M., Yi, W., Myer, L.R. & Cook, N.G.W. 1999. Fracture channel waves. *J. Geophys. Res.* 104:4769-4781.

Nihei, K.T., Goldstein, P., Myer, L.R. & Mayeda, K. 2000. Natural fracture characterization using passive seismic waves. *GasTIPS* 6(1):21-25.

Pyrak-Nolte, L.J., Myer, L.R. & Cook, N.G.W. 1990. Transmission of seismic waves across single natural fractures. *J. Geophys. Res.* 95:8617-8638.

Pyrak-Nolte, L.J., Xu, J. & Haley, G.M. 1992. Elastic interface waves propagating in a fracture. *Phys. Rev. Lett.* 68:3650-3653.

Schoenberg, M. 1980. Elastic wave behavior across linear slip interfaces. *J. Acoust. Soc. Am.* 68:1516-1521.

Schoenberg, M. & Sayers, C.M. 1995. Seismic anisotropy of fractured rock. *Geophys.* 60(1):204-211.

Tarantola, A. 1988. Theoretical background for the inversion of seismic waveforms including elasticity and attenuation. *Pure and Appl. Geophys.* 128:365-399.

Tsvankin, I. & Lynn, H.B. 1999. Special section on azimuthal dependence of P-wave seismic signatures - Introduction. *Geophys.* 64:1139-1142.